CHEMISTRY JOURNAL OF MOLDOVA. General, Industrial and Ecological Chemistry. 2025, 20(2), 33-44
ISSN (p) 1857-1727 ISSN (e) 2345-1688
http://cjm.ichem.md
https://doi.org/10.19261/cjm.2025.1344

COMPARATIVE STUDY OF MgO NANOPARTICLES SYNTHESIZED IN THE PRESENCE OF SODIUM DODECYL SULPHATE AND ALOE VERA

Mariana Diru*, Ion Lungu, Tamara Potlog

Institute of Applied Physics, Moldova State University, 5, Academiei str., Chisinau MD 2028, Republic of Moldova
**e-mail: mariana.diru@usm.md*

Abstract. Magnesium oxide (MgO) nanoparticles were synthesized using two distinct stabilizing agents-sodium dodecyl sulphate (SDS) and Aloe Vera extract (AVE)-in order to evaluate how electrostatic versus biopolymeric stabilization affects nucleation, crystallite formation, and final structural properties. The nanoparticles were obtained through a precipitation route followed by calcination at 500–1100°C. XRD analysis confirmed the formation of nanocrystalline MgO, with the crystallite size being slightly influenced by the choice of stabilizing agent. SDS promoted electrostatic micellar templating, resulting in faster nucleation and smaller but defect-richer crystallites, whereas Aloe Vera acted as a steric capping agent that delayed supersaturation and enabled more ordered crystal growth. FTIR and XPS analyses revealed temperature-dependent dehydroxylation and surface carbonation effects, consistent with nanoscale MgO chemical reactivity. The optical bandgap ranged from 5.4 to 6.0 eV, exhibiting a blue shift relative to bulk MgO due to nanoscale confinement and surface defect states. Overall, the results demonstrate that the precipitation environment plays a decisive role in controlling MgO crystallization kinetics, defect chemistry, and nanoparticle stability, with Aloe Vera providing superior steric stabilization against agglomeration compared to SDS.

Keywords: MgO nanoparticles, sodium dodecyl sulphate, Aloe Vera, the coprecipitation method.

Received: 19 August 2025/ Revised final: 10 December 2025/ Accepted: 12 December 2025

Introduction

In recent years, significant progress has been made in the design and synthesis of MgO nanoparticles (NPs). MgO NPs represent a category of nanomaterials that have found applications across diverse fields such as biosensing technology [1], tissue engineering [2], catalysis [3], food packaging [4], biomedicine [5], and environmental sciences [6]. MgO NPs possess several favourable physicochemical characteristics, including enhanced ionic character, substantial specific surface area, distinctive crystalline structures, and oxygen vacancies, allowing efficient interaction with various biological systems [7–10].

MgO exists as an "infinite" ionic lattice composed of Mg^{2+} and O^{2-} ions in a 1:1 ratio, arranged such that each ion is surrounded by six ions of opposite charge, resulting in a completely ionic lattice. Due to its ionic bonding, MgO is soluble in water. Additionally, it has been reported that MgO nanocatalysts have a specific surface area of approximately 60.2 m^2/g [11], compared to the 19 m^2/g surface area of larger MgO particles. Furthermore, MgO 3D-flowers exhibit a specific surface area of 218 m^2/g [1]. The synthesis techniques employed are responsible for producing various defects in metal oxides, thereby altering their behaviour.

Different kinds of MgO nanostructures have been fabricated using a variety of methods [12,13]. Some authors [14] have obtained them by direct current (DC) arc plasma jet chemical vapour deposition (CVD). The growth time does not exceed 10 minutes using this synthesis method, and the growth rate of DC arc plasma jet CVD is much higher than that of other methods [15]. MgO nanowires have been synthesized through a vapor-phase precursor method [16]. Highly luminescent magnesium oxide nanocrystallites have been synthesized by the sol-gel method [17]. In general, MgO nanoparticles have been synthesized using a variety of physical, chemical, and green approaches [18–23].

In this study, were comparatively evaluate MgO NPs synthesized using sodium dodecyl sulphate (SDS) and Aloe Vera extract (AVE) as dispersing/capping agents, where SDS plays the role of an anionic surfactant that forms micelles to electrostatically stabilize the nuclei of $Mg(OH)_2$ during precipitation and prevent their uncontrolled agglomeration. In contrast, Aloe Vera extract acts as a natural capping agent as it contains polysaccharides and hydroxyl-rich biomolecules

capable of weakly coordinating Mg^{2+} ions, thereby providing steric stabilization of the nascent nuclei. Unlike conventional surfactants, Aloe Vera does not participate as a reducing agent but rather modulates the morphology and particle size distribution through biomolecular surface passivation.

Experimental

Materials

Reagents with analytical grade were used for the synthesis. $Mg(NO_3)_2 \cdot 6H_2O$, $NaC_{12}H_{25}SO_4$, NaOH and Aloe Vera were purchased from Sigma-Aldrich. All solutions were prepared using distilled water.

Synthesis of magnesium hydroxide

The production of MgO nanoparticles was carried out in two stages: a) synthesis of magnesium hydroxide and b) thermal treatment of magnesium hydroxide.

For the synthesis of magnesium hydroxide, the precipitation method was used, which is simple and cost-effective. $Mg(NO_3)_2 \cdot 6H_2O$ and NaOH were used as precursors, while SDS and AVE were used as dispersing agents. All chemical reagents were of analytical grade and used without further purification. The concentration of NaOH critically determines the balance between nucleation and growth. A high OH^- availability rapidly exceeds the Ksp threshold, causing instantaneous 'burst' nucleation and producing a high density of small $Mg(OH)_2$ nuclei. Under lower OH^- availability, nucleation proceeds more gradually, and the subsequent particle growth becomes diffusion-controlled, which typically yields better crystallinity and larger primary domains after calcination. In Aloe Vera-mediated synthesis, the initial complexation of Mg^{2+} further delays OH^--driven nucleation, reinforcing the controlled-growth regime.

Synthesis of MgO NPs with SDS

Procedure 1 - A magnesium nitrate solution was first prepared by dissolving 5.000 g of $Mg(NO_3)_2 \cdot 6H_2O$ in 100 mL of distilled water. Subsequently, an SDS solution prepared by dissolving 0.288 g of $NaC_{12}H_{25}SO_4$ in distilled water was added dropwise to the magnesium nitrate solution under continuous stirring. In parallel, a NaOH solution was prepared by dissolving 0.800 g of NaOH in distilled water. The SDS solution was added in small portions to the magnesium nitrate solution under stirring. Subsequently, the NaOH solution was added dropwise under continuous stirring at a temperature of 70–80°C for 2 hours. The formation of a white precipitate was observed according to the reactions described in Eqs.(1–4).

$$NaC_{12}H_{25}SO_4 \rightarrow Na^+ + C_{12}H_{25}SO_4^- \quad (1)$$

$$NaOH \rightarrow Na^+ + OH^- \quad (2)$$

$$Mg(NO_3)_2 \rightarrow Mg^{2+} + 2NO_3^- \quad (3)$$

$$Mg^{2+} + 2OH^- \leftrightarrow Mg(OH)_2\downarrow \quad (4)$$

The precipitate was filtered using blue-banded filter paper and washed with 50 mL of distilled water. It was then dried at room temperature, with a synthesis yield of 66.7%.

Procedure 2 - The synthesis procedure was the same as in Procedure 1, except the amount of SDS added was modified to 0.057 g, with a synthesis yield of 51.1%.

Synthesis of MgO NPs with AVE

Procedure 3 - A quantity of 100 mL of magnesium nitrate solution was prepared by dissolving 5.000 g of $Mg(NO_3)_2 \cdot 6H_2O$ in distilled water, and a NaOH solution was prepared by dissolving 2.000 g of NaOH in distilled water. While stirring the magnesium nitrate solution, 15 mL of 99.5% AVE was added in small portions. Subsequently, the NaOH solution was added dropwise under continuous stirring at a temperature of 70–80°C for 2 hours. A white precipitate was formed, which was filtered using blue-banded filter paper and washed with 50 mL of distilled water. The precipitate was dried at room temperature, with a synthesis yield of 1.322 g.

Procedure 4 - The synthesis procedure was the same as in Procedure 3, except the amount of AVE added was modified to 10 mL. The synthesis yield was 1.369 g.

Thermal treatment of magnesium hydroxide

After drying at room temperature, the magnesium hydroxide samples were heat-treated in the temperature range of 500–1100°C.

Instruments

The structure of the MgO NPs composite was investigated by X-ray diffraction (XRD) using a Bruker-AXS D8 Advance diffractometer (CuKα radiation, 40 mA, 40 kV). The morphology and composition were examined using a TESCAN Vega TS 5130 MM (Brno, Czech Republic) scanning electron microscope (SEM) equipped with an energy-dispersive X-ray (EDX) analyzer (Oxford, UK) operated at 20 kV. A Bruker Alpha FTIR spectrometer with a Diamond Crystal ATR accessory was used for rapid compound identification. The chemical composition of the MgO NPs compounds was further analyzed using an FT-IR 4600 spectrometer (Spectrum Research Systems Co.) in the mid-infrared region, ranging from 4000 to 400 cm^{-1}. UV-Vis spectroscopy was performed using a Cary 300 UV-Vis spectrophotometer (Agilent Technologies) in the spectral range of 200–800 nm.

Results and discussion

Composition of MgO NPs

The SEM-EDS technique was used to provide qualitative information about the elements present in the MgO NPs. The EDS analysis (Table 1) shows that the MgO metal oxide synthesized with 0.288 g of SDS consists of Mg and O atoms at different concentrations, depending on the annealing temperature. As the concentration of SDS in the solutions decreased, an increase in oxygen content and a decrease in the concentration of Mg atoms were observed (Table 2).

The comparison of the composition of MgO synthesized with the highest SDS content and calcined at 700°C for the same duration indicates that the concentration of Mg atoms decreased compared to those with a lower SDS content. The best stoichiometry of the MgO NPs was obtained with 0.057 g of SDS, while for NPs synthesized with 0.288 g of SDS under different calcination conditions, an almost identical composition was observed.

The difference between the atomic ratios obtained by EDS and XPS arises from the distinct probing depths of the two techniques. While EDS collects bulk information from hundreds of nanometers into the sample, XPS probes only the outermost 5–10 nm. This surface layer is enriched in oxygen-containing species such as hydroxyls, adsorbed water, and carbonates, which preferentially accumulate on MgO surfaces due to their high basicity. Therefore, the O-rich surface signature observed by XPS does not indicate nonstoichiometric bulk MgO, but rather typical surface hydroxylation and carbonation effects. The survey XPS spectra of the MgO NPs synthesized with SDS as the dispersing agent, measured in the first atomic layers (~10 nm) and presented in Figure 1 across the entire binding energy range, showed characteristic peaks for C 1s, O 1s, O 2s, Mg 1s, Mg 2s, and Mg 2p. Similar elements, with slight shifts, were also observed in the MgO NPs synthesized with AVE as the dispersing agent.

Table 1

Composition of MgO NPs with 0.288 g of SDS.

MgO NPs	*T, ℃*	*t, h*	*Atomic %*			
			EDX		*XPS*	
			Mg	*O*	*O*	*Mg*
LS-2-0	-	-	37.62	62.38	62.09	37.91
LS-2-1	500	4	44.15	55.85	-	-
LS-2-2	700	4	43.73	56.27	47.77	52.23
LS-2-3	700	6	46.82	53.18	44.91	55.09
LS-2-4	500	6	46.78	53.22	56.61	45.09
LS-2-6	1060	15	44.35	55.65	-	-

Table 2

Composition of MgO NPs with 0.057 g of SDS.

MgO NPs	*t, ℃*	*t, h*	*Atomic %*			
			EDX		*XPS*	
			Mg	*O*	*O*	*Mg*
LS-3-0	-	-	35.51	64.49	59.61	40.39
LS-3-1	700	6	46.93	53.07	45.10	54.9
LS-3-2	500	6	39.24	60.76	-	-
LS-3-3	300	6	32.27	67.72	-	-

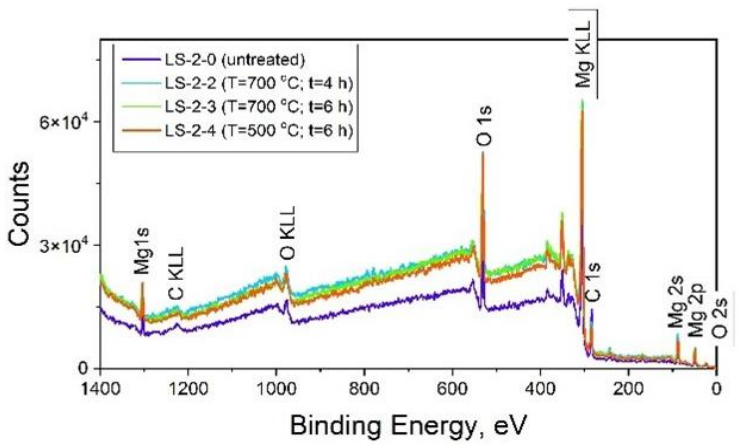

Figure 1. Survey XPS spectrum of MgO NPs with SDS precipitating agent.

The C 1s peaks confirm the XPS measurement results and reveal two distinct peaks corresponding to carbon species. The C 1s spectra for both MgO NPs (synthesized with SDS - Figure 2 and AVE - Figure 3) are well-fitted with two Gaussian components. The first peak consistently appears at around 284.2 eV and is attributed to carbon atoms bonded exclusively to other carbon atoms (C–C). For samples calcined at different temperatures, this peak shifts to 285 eV and 287 eV, respectively. The second peak, initially located at 287 eV for the as-grown samples, is typically assigned to carbon atoms bonded to one oxygen atom (C–O). For MgO NPs synthesized with SDS and calcined at different temperatures, this second peak shifts slightly to the 287.8–290.1 eV range (300–500°C), while for MgO NPs synthesized with AVE and calcined at 700°C, the second peak shifts to 292.3 eV.

In the samples synthesized with different precipitating agents, the peak positions and shapes of the Mg 1s and Mg 2p signals do not coincide but are consistent with the presence of Mg(II) species [24-28]. The fitting procedure reveals the presence of a single contribution attributed to Mg(II) in magnesium oxide/hydroxide. This is observed in Figure 4 and Figure 5, in both the as-grown samples, at 1303 eV for the Mg 1s signal, and in the calcined samples, where the peak shifts to 1304 eV and 1305 eV due to the formation of magnesium carbonate species [29].

Figure 6 and Figure 7 show the high-resolution singlet peaks for the Mg 2p regions of MgO NPs synthesized with SDS and AVE as precipitating agents. A slight shift to higher binding energies and an increase in peak intensity with increasing calcination temperature are observed in the XPS spectra of the Mg 2p regions. In the Mg 2p regions, within the ranges of 48.9–50.2 eV and 49–51 eV for MgO NPs synthesized with SDS and AVE, respectively, only the contribution from magnesium oxide/hydroxide is evident [30–32].

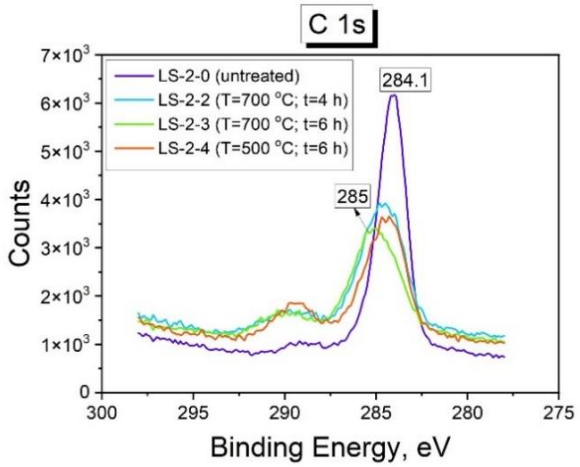

Figure 2. XPS spectra of the C 1s regions of MgO synthesized with SDS precipitation agents.

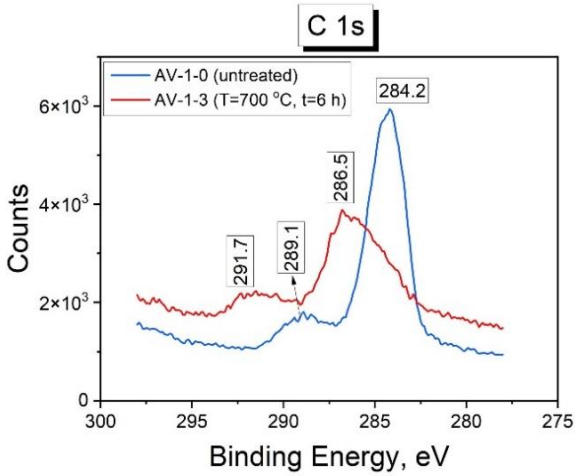

Figure 3. XPS spectra of the C 1s regions of MgO synthesized with AVE precipitation agents.

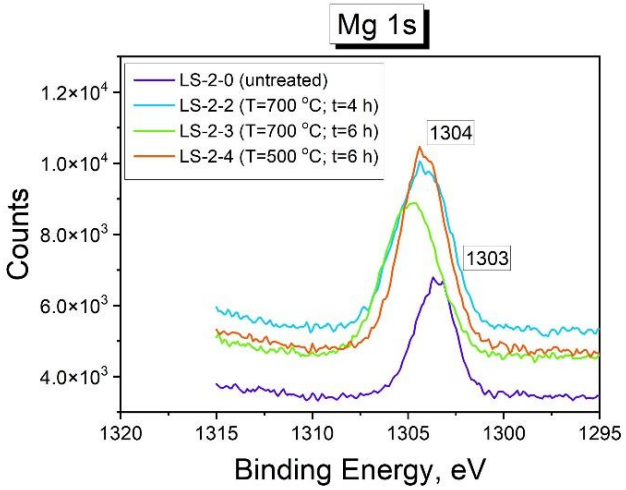

Figure 4. XPS spectra of Mg1s regions of MgO NPs with SDS precipitation agent.

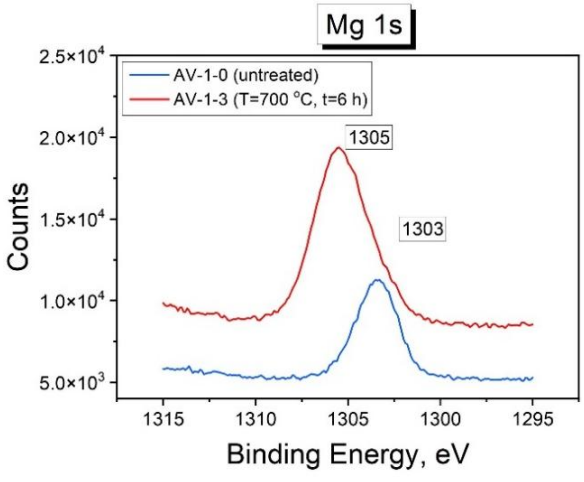

Figure 5. XPS spectra of Mg1s regions of MgO NPs with AVE precipitation agent.

The O 1s spectra of as-grown MgO NPs presented in Figure 8 and Figure 9, obtained using different precipitating agents, show a peak at 530.8 eV, which is attributed to MgO. For MgO synthesized with SDS and calcined at different temperatures, the presence of oxygen corresponds to $Mg(OH)_2$. The O 1s spectrum of calcined MgO NPs synthesized with AVE is located at 532 eV and is consistent with oxygen in $MgCO_3$ [33].

The minor $MgCO_3$-related features observed in some samples can originate from the carbonization of Aloe Vera polysaccharides during the initial stages of calcination, generating CO_2 that subsequently reacts with MgO at the surface. Additionally, the high surface basicity and hydroxylation degree of nanoscale MgO promote atmospheric CO_2 adsorption, further contributing to the formation of surface carbonates. These carbonate residues progressively diminish above 700°C, where complete dehydration and decarboxylation enhance the phase purity of MgO.

The precipitation of $Mg(OH)_2$ is governed by the solubility product constant ($K_{sp} \approx 6 \times 10^{-12}$), which is rapidly exceeded in SDS-containing solutions due to the higher ionic strength introduced by Na^+ and SO_4^{2-} ions. This accelerates the supersaturation threshold, resulting in rapid nucleation. In contrast, Aloe Vera forms a low-ionic-strength microenvironment in which Mg^{2+} ions are partially coordinated by organic ligands before OH^- addition, delaying supersaturation and yielding a slower, more controlled nucleation pathway. This mechanistic difference explains the smaller crystallite dispersion, but slightly larger average crystal size obtained for AVE-assisted precipitation compared to SDS-assisted synthesis.

The EDS and XPS analyses confirm that both stabilization pathways lead to the formation of nanoscale MgO. It is evident that the Mg/O atomic ratio obtained from these results is in good agreement. A slightly higher oxygen atomic ratio compared to that of magnesium is probably due to the absorption of moisture from the environment. In addition, the O-rich signature detected by XPS can also be attributed to surface hydroxylation and adsorbed moisture, which are thermodynamically favoured on basic MgO surfaces and become progressively reduced at higher calcination temperatures. This further confirms that the excess oxygen detected by XPS originates from surface termination effects rather than bulk non-stoichiometry.

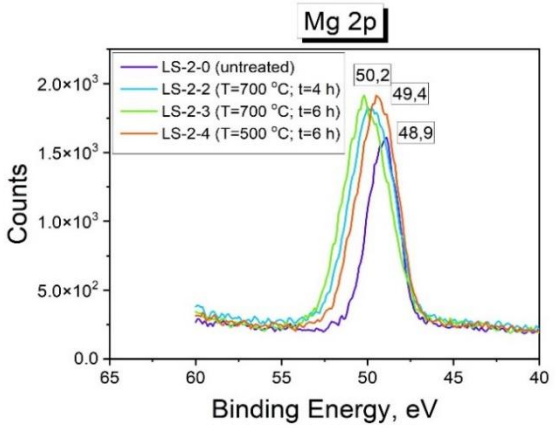

Figure 6. XPS spectra of the Mg 2p regions of MgO NPs with SDS precipitation agent.

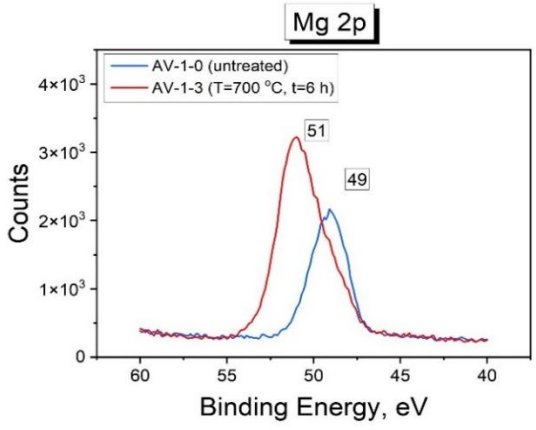

Figure 7. XPS spectra of the Mg 2p regions of MgO NPs with AVE precipitation agent.

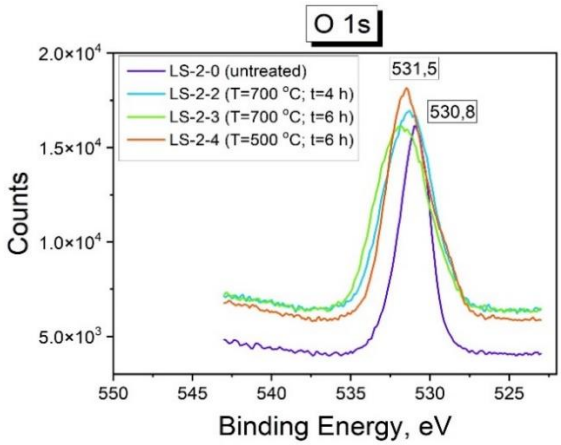

Figure 8. XPS spectra of the O 1s regions of MgO NPs with SDS precipitation agent.

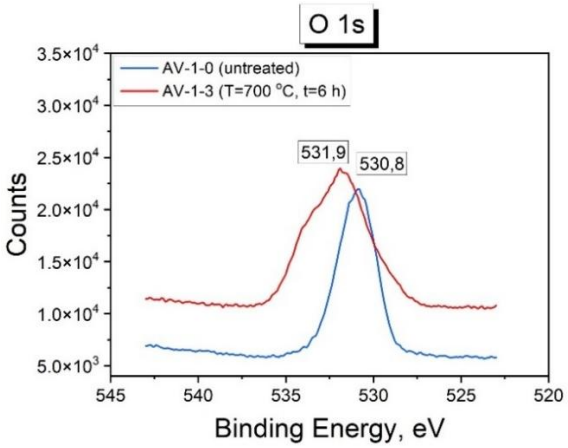

Figure 9. XPS spectra of the O 1s regions of MgO NPs with AVE precipitation agent.

The interaction between Mg^{2+} and Aloe Vera components occurs prior to precipitation, through weak coordination with hydroxyl, carbonyl and carboxyl functional groups of polysaccharides such as acemannan and glucomannan. These biomolecules act as soft ligands that partially chelate Mg^{2+} ions in solution, reducing the supersaturation degree and moderating the nucleation step. As a result, the initial nuclei are sterically stabilized, which leads to improved dispersion and narrower crystallite size distribution after thermal conversion to MgO.

The different nucleation environments generated by SDS and Aloe Vera also explain the distinct morphological evolution of nanoparticles. In SDS-containing systems, anionic micelles act as soft templates that concentrate Mg^{2+} ions at their interface, accelerating supersaturation and promoting rapid nucleation, which results in smaller and defect-richer crystallites. In contrast, Aloe Vera does not form micelles but stabilizes nuclei through steric shielding by polysaccharides, delaying nucleation and allowing slower, more ordered crystal growth. Thus, SDS governs morphology through electrostatic micellar templating, whereas Aloe Vera controls it through biomolecular surface passivation.

FTIR spectra of the MgO nanoparticles were recorded at room temperature in the 400–4000 cm^{-1} range. Figure 10 presents the spectra of as-grown MgO synthesized with SDS as the precipitating agent and subsequently calcined at different temperatures. In the as-grown sample, a characteristic band at ~427 cm^{-1} indicates the Mg–O lattice vibration, confirming the presence of the oxide phase. The broad feature at ~3696 cm^{-1} is attributed to O–H stretching modes arising from surface hydroxyl groups, while the band at 1061 cm^{-1} corresponds to Mg–OH vibrations [34,35], which may also overlap with C–H out-of-plane bending modes associated with residual organic fragments.

FTIR spectra for MgO NPs annealed at different temperatures show slight changes in intensity and small shifts in the vibration modes with increasing calcination temperature. Peaks appearing between 400–700 cm^{-1} confirm the presence of MgO at the nanoscale. The band at ~420–450 cm^{-1} corresponds to the intrinsic Mg–O stretching vibration in the rock-salt lattice, confirming the formation of the oxide phase. The broader feature at ~850–880 cm^{-1} is attributed to Mg–O–Mg bridging units, which become more pronounced as crystallinity improves with temperature.

The absorption in the 1400–1500 cm^{-1} region originates from surface carbonates formed through CO_2 adsorption on hydroxylated MgO surfaces, a behaviour characteristic of highly basic oxide nanomaterials. Meanwhile, the O–H stretching feature near 3600–3700 cm^{-1} reflects residual hydroxyl groups present at lower calcination temperatures; these vanish progressively above 700°C as dehydration is completed. The stretching vibration mode around 860–867 cm^{-1} indicates Mg–O–Mg bonds. Distinct bands observed between ~1420–1438 cm^{-1} denote the bending vibration of surface hydroxyl groups. A broad band at around 2980 cm^{-1} in MgO NPs calcined at 500°C is attributed to aliphatic C–H stretching. The broad band between 1413–1461 cm^{-1} for MgO NPs synthesized with the AVE precipitating agent (Figure 11) is due to C–H asymmetric stretching.

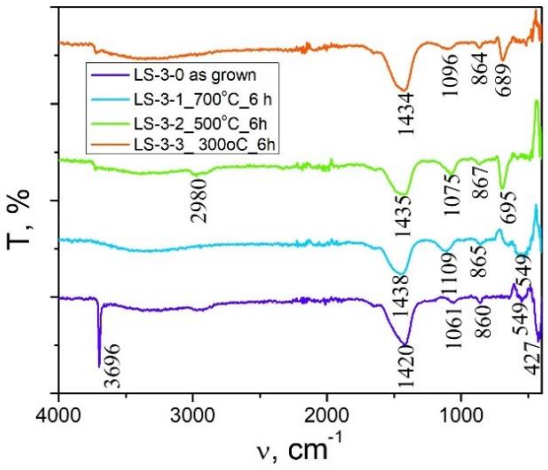

Figure 10. FTIR spectra of MgO NPs with SDS precipitation agent.

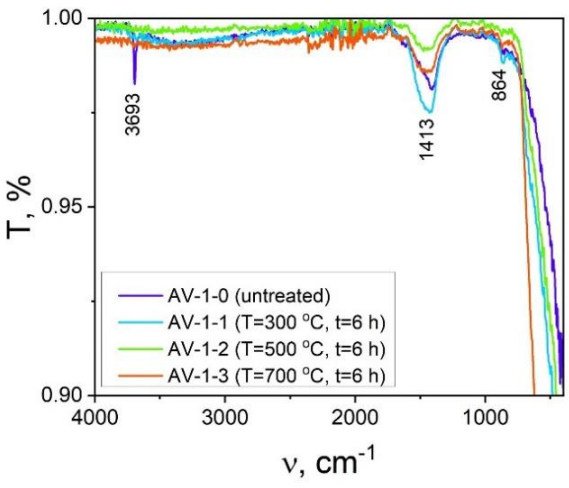

Figure 11. FTIR spectra of MgO NPs with AVE precipitation agent.

X-ray diffraction (XRD) was performed in the range of 10°–80° (2θ) using CuKα radiation. XRD analysis allows for the comparison of differences in the crystal structure of MgO NPs synthesized with SDS and AVE as precipitating agents. Figure 12 and Figure 13 show the X-ray diffraction patterns of the synthesized MgO NPs using SDS and AVE as precipitating agents.

The effects of various parameters, such as temperature and calcination time, on the quality of the MgO NPs were evaluated. Notably, almost the same diffraction peaks were indexed for both as-grown MgO NPs synthesized with SDS and AVE as precipitating agents, corresponding to the $Mg(OH)_2$ phase. The XRD patterns of MgO NPs synthesized with the SDS precipitating agent at 500°C and 700°C (Figure 12) with a calcination time of 4–6 hours showed only MgO peaks, indicating the complete formation of pure nanocrystalline MgO. However, the broadness of the peaks suggested the presence of impurities. With further increases in temperature to 700–1060°C or calcination time to 11–15 hours (Figure 12), sharp peaks appeared that matched well with the JCPDS data (89-7746) and showed no foreign impurities. The minor carbonate-related reflections observed for some samples do not originate from incomplete conversion of $Mg(OH)_2$, but from post-synthesis surface carbonation. Due to the strong basicity of MgO surfaces, freshly calcined nanoparticles readily adsorb atmospheric CO_2, forming a thin surface layer of $MgCO_3$-type species. This assignment is supported by the fact that these reflections weaken or disappear at higher calcination temperatures, where re-carbonation is kinetically suppressed. Therefore, the presence of $MgCO_3$ is attributed to surface adsorption rather than an unconverted intermediate phase.

The XRD data suggested a cubic structure with an average crystallite size of 26 nm, which is in good agreement with results reported by other authors [36,37]. The average crystallite size, calculated using the Debye-Scherrer equation for the most intense peaks corresponding to the (200) and (220) planes of MgO nanoparticles at 500°C and 700°C with a calcination time of 4 hours, was 12.4 nm and 21.7 nm, respectively. For a calcination time of 6 hours at 500°C and 700°C, the crystallite sizes decreased to 9.96 nm and 18.94 nm, respectively.

The calcination time also plays a decisive role in structural ordering. Shorter thermal treatments preserve a higher concentration of lattice and surface defects, which manifest as broader diffraction peaks due to microstrain. When the calcination time is extended, diffusion-driven recrystallization reduces defect density and results in peak sharpening. However, overly long calcination promotes grain coarsening, which decreases the specific surface area even though the crystallinity improves.

The XRD patterns of MgO nanoparticles synthesized using Aloe Vera extract as the precipitating agent and calcined at 500°C and 700°C for 4–6 hours are shown in Figure 13. With increasing calcination temperature, the diffraction peaks become more intense while maintaining their positions, indicating enhanced crystallinity without any change in lattice symmetry. A slight increase in crystallite size was also observed compared to the samples obtained *via* the SDS-assisted route. This phase transformation proceeds through a lattice dehydroxylation mechanism: the brucite-type lamellar structure of $Mg(OH)_2$ becomes destabilized as structural water is released between 350–450°C, generating oxygen vacancies and initiating cation rearrangement.

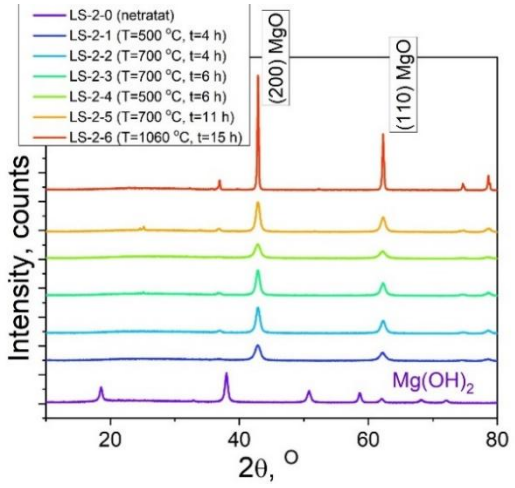

Figure 12. The X-ray diffraction pattern of the MgO NPs with SDS precipitation agent.

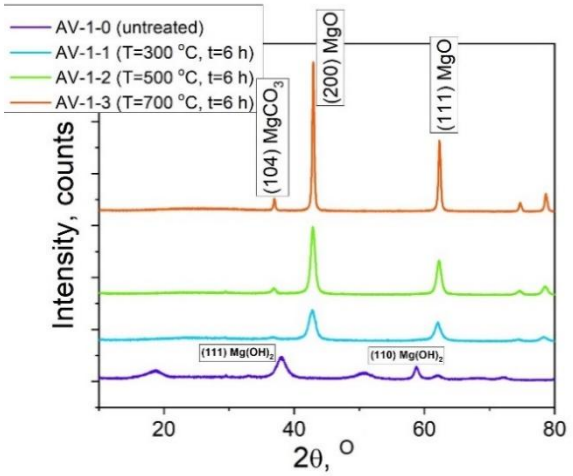

Figure 13. The X-ray diffraction pattern of the MgO NPs with AVE precipitation agent.

With increasing temperature (≥500–700°C), these vacancies reorder into the thermodynamically stable rock-salt cubic phase of MgO. The collapse of the layered hydroxide structure and the subsequent densification of the oxygen sublattice are responsible for the emergence of the fully developed MgO phase.

Comparable findings are presented in Table 3, which also includes the microstructural parameters of commercial MgO NPs. The average crystallite size of the MgO NPs was estimated using the Scherrer formula. The data indicates that the average crystallite size of the synthesized MgO NPs is slightly influenced by the precipitating agent. However, the average crystallite size of the commercial MgO NPs is approximately twice as large as that of the synthesized ones.

To further validate the crystallite size evaluation, both the Scherrer and Williamson–Hall (W–H) approaches were applied. The values obtained from the two methods were found to be consistent, confirming that peak broadening is primarily governed by crystallite size rather than lattice distortion. Unlike the Scherrer equation, which includes instrumental broadening in β, the W–H method separates size and strain effects, allowing a more reliable estimation of microstrain (ε). The calculated strain values were higher in the as-grown and low-temperature samples and progressively decreased with longer calcination time and higher temperature, which is consistent with thermally induced defect relaxation and recrystallization. This correlation confirms that the defect-driven peak broadening observed at lower calcination stages is gradually suppressed as the oxides become structurally ordered.The same diffraction planes were observed for the MgO NPs synthesized with the AVE precipitating agent as in the case of the commercial nanoparticles, with the only difference being the crystallite size. In Figure 13, the XRD patterns of the MgO NPs synthesized with the AVE precipitating agent, in comparison with those synthesized with SDS, revealed the presence of both the $Mg(OH)_2$ phase and additional $MgCO_3$ peaks.

The selected calcination interval (500–1100°C) reflects the thermochemical pathway of $Mg(OH)_2$ decomposition. Below ~400°C, dehydration is incomplete, and the hydroxide phase dominates. Between 450–700°C, structural rearrangement leads to the formation of nanocrystalline MgO. At higher temperatures (≥900°C), recrystallization becomes dominant, improving long-range order and reducing residual surface carbonates. Minor transient $MgCO_3$ species may form either from decomposing Aloe Vera organics or from atmospheric CO_2 adsorption on hydroxyl-rich surfaces, but they are eliminated at elevated temperatures, yielding highly crystalline MgO.

Table 3

Comparative microstructural parameters of synthesized and commercial MgO NPs.

MgO NPs with SDS precipitation agent, calcination T, °C= 500, 6 h			*MgO NPs with AVE precipitation agent, calcination T, °C= 500, 6 h*			*Commercial MgO NPs [7]*		
2θ (deg)	*Diffraction planes*	*Crystallite size, nm*	*2θ (deg)*	*Diffraction planes*	*Crystallite size, nm*	*2θ (deg)*	*Diffraction planes*	*Crystallite size, nm*
			36.87	(111)	12.91	36.86	(111)	37.6
42.84	(200)	13.68	42.87	(200)	11.20	42.78	(200)	19.5
62.20	(220)	8.81	62.23	(220)	11.09	62.12	(220)	19.8
74.58	(311)	7.99	74.59	(311)	10.72	74.50	(311)	16.7
78.53	(222)	10.06	78.53	(222)	11.26	78.43	(222)	17.6
The average crystallite size, nm		10.14			11.44			22.24

Table 4

Comparison of Williamson–Hall microstrain with apparent strain inferred from Scherrer broadening for MgO nanoparticles synthesized with SDS and AVE.

Sample (SDS)	*ε (W–H)*	*ε (Scherrer)*	*Sample (AVE)*	*ε (W–H)*	*ε (Scherrer)*
LS-2-0	*1.76*	*6.8*	*AV-1-0*	*3.99*	*18.15*
LS-2-1	*0.35*	*6.6*	*AV-1-1*	*9.36*	*11.4*
LS-2-2	*2.75*	*5.6*	*AV-1-2*	*1.18*	*6.7*
LS-2-3	*2.75*	*5.7*	*AV-1-3*	*1.39*	*3.2*
LS-2-4	*3.84*	*8.9*			
LS-2-5	*3.08*	*6.5*			
LS-2-6	*2.90*	*2.9*			

The thermal evolution of the material can be clearly tracked using the combined FTIR and XRD evidence. The gradual disappearance of Mg–OH vibrational bands and the emergence of the characteristic Mg–O lattice modes above 500–700°C, together with the progressive sharpening of the diffraction peaks, indicate the structural rearrangement from $Mg(OH)_2$ to MgO. These complementary spectroscopic and structural signatures confirm the complete phase transformation solely based on FTIR and XRD data.

Optical properties of MgO with SDS and AVE precipitating agents

Figure 14 shows the UV–Visible absorption spectra of MgO NPs synthesized with SDS as the precipitating agent near the absorption edge at different temperatures and calcination times. The absorbance spectra clearly indicate that all MgO NPs absorb light in the visible spectrum. The evaluated bandgap values (5.4–6.0 eV) are in good agreement with those reported for nanostructured MgO synthesized *via* precipitation or biogenic routes (typically 5.2–6.2 eV) [38]. The slight difference between SDS- and AVE-assisted samples originates from microstructural effects, namely defect density and crystallite size-rather than from changes in the electronic structure of the oxide lattice. This also explains the deviation from the bulk bandgap of MgO (~7.8 eV), which is seldom observed in nanoscale systems where the band structure is dominated by surface-state and confinement-induced modifications.

The optical properties are also influenced by oxygen-related surface defects, which are intrinsic to nanoscale MgO. These non-stoichiometric oxygen sites introduce shallow states that slightly modify the electronic structure near the band edge and contribute to the observed blue-shift. Samples synthesized with SDS exhibit a higher initial concentration of such defect-related states due to rapid nucleation, while Aloe Vera assisted synthesis promotes slower crystallization and partial defect equilibration. The progressive reduction of these defects with increasing calcination temperature is consistent with the narrowing of optical variability and the stabilization of the bandgap.

For a direct band gap semiconductor with allowed band-to-band transitions, the optical energy gap (*Eg*) was estimated from the absorption spectra using the relation $(\alpha h\nu)^2 = f(h\nu)$ (Figure 15). The band gap energies for the MgO NPs synthesized with the SDS precipitating agent were determined to be 5.40 eV for the as-grown sample and 6.03 eV for the sample calcined at 1060°C.

In Figure 16 and Figure 17, the absorbance spectra and the $(\alpha h\nu)^2 = f(h\nu)$ dependencies of MgO NPs synthesized with the AVE precipitating agent are presented.

The absorption peaks of both MgO NPs exhibits a blue shift. The observed optical blue shift relative to bulk MgO originates from a combination of nanoscale effects and defect-mediated electronic restructuring. At reduced crystallite sizes, the electronic charge carriers become spatially confined within the nanocrystal volume, which increases the effective bandgap energy according to the quantum size effect. In addition to confinement, the large surface-to-volume ratio introduces under-coordinated oxygen sites and surface hydroxyls that alter the local potential landscape at the band edges. These surface states slightly shift the conduction band upward while simultaneously suppressing the tailing of the valence band, which amplifies the apparent blue shift. Therefore, the optical transition edge is not only a size-dependent property but also reflects the defect chemistry and surface termination of the nanoparticles.

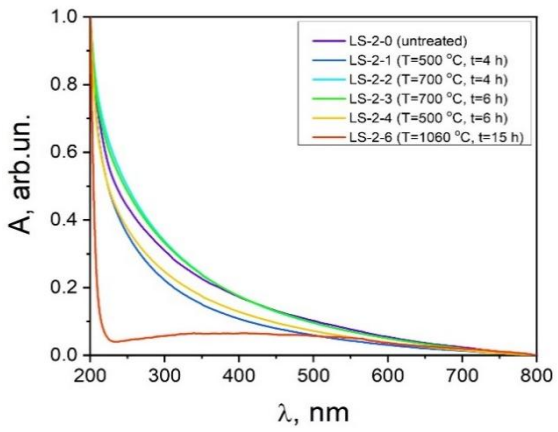

Figure 14. The absorbance spectra of MgO NPs synthesized with SDS as the precipitating agent.

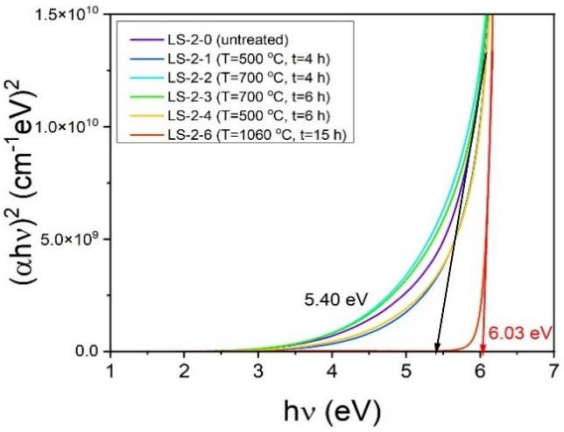

Figure 15. The $(\alpha h\nu)^2 = f(h\nu)$ dependencies of MgO NPs synthesized with SDS as the precipitating agent.

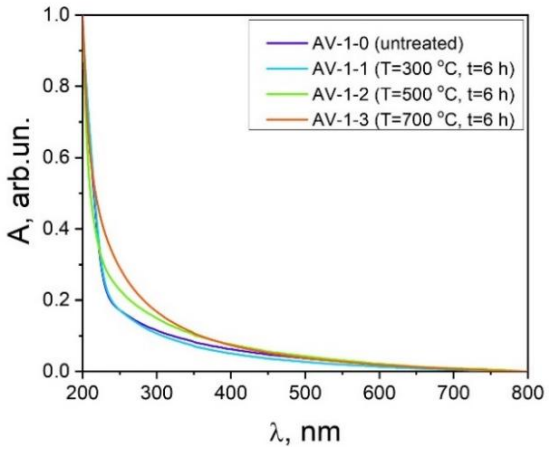

Figure 16. The absorbance spectra of MgO NPs synthesized with AVE as the precipitating agent.

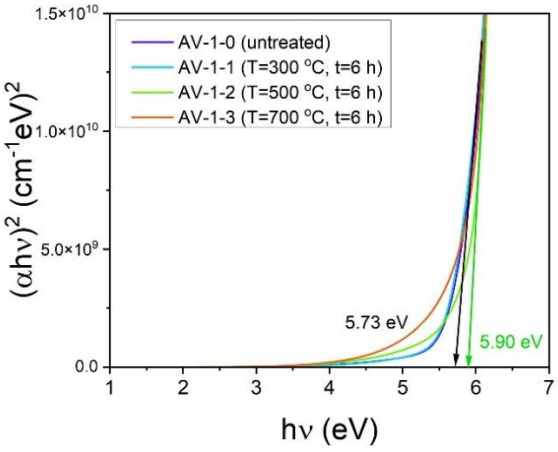

Figure 17. The (αhν)²= f(hν) dependencies (b) of MgO NPs synthesized with AVE as the precipitating agent.

Table 5

Comparative role of SDS and Aloe Vera as stabilizing agents during MgO nanoparticle formation.

Parameter	*SDS route*	*Aloe Vera route*
Stabilization mechanism	Electrostatic (micelle templating)	Steric (biopolymer shielding)
Nucleation rate	Very fast (burst nucleation)	Moderated (complexation-controlled)
Crystallite size	Smaller	Slightly larger but better ordered
Defect concentration	Higher initially	Lower due to gradual ordering
Agglomeration	More likely secondary	Reduced via steric hindrance

This effect gradually moderates higher calcination temperatures, where defect annihilation and partial grain growth reduce surface-state contributions to the band structure. For the as-grown nanoparticles, the absorbance shows a peak at 214 nm. This absorption is significantly higher than that of bulk MgO, which exhibits excitonic transitions for single crystals at 163 nm. The evaluated optical band gap energy of the as-grown MgO NPs is 5.73 eV, which agrees well with values reported in other studies [41]. With increasing calcination temperature up to 500°C, the band gap increases to 5.9 eV. However, with further increases in calcination temperature, the band gap decreases back to the value obtained for the as-grown MgO NPs. A similar trend was observed for MgO NPs synthesized with the SDS precipitating agent.

The distinct stabilization mechanisms of SDS and Aloe Vera directly influence the resulting nanoparticle size distribution and tendency toward agglomeration. SDS provides electrostatic stabilization through anionic micellar templating, which accelerates supersaturation and yields smaller crystallites, but also traps a higher density of structural defects. Aloe Vera, in contrast, acts as a steric stabilizer through polysaccharide-rich biomolecules that coordinate Mg^{2+} prior to precipitation, slowing nucleation and enabling more ordered growth while preventing severe agglomeration. A concise comparison is provided in Table 5.

Conclusions

The current study focused on the synthesis of magnesium oxide nanoparticles. The two precipitating agents exhibited distinct stabilization mechanisms that influenced the nanoparticle growth pathway. SDS acted through electrostatic micellar templating, which accelerated nucleation and yielded smaller crystallites with a higher initial defect concentration. In contrast, Aloe Vera provided steric stabilization *via* its polysaccharide matrix, leading to slower nucleation, improved crystalline ordering, and reduced agglomeration. These mechanistic differences account for the slight variations in crystallite size and optical properties between the two routes. The MgO nanoparticles were characterized using scanning electron microscopy, X-ray diffraction, and infrared spectroscopy. The experimental data indicate that the average crystallite size of the synthesized MgO NPs is slightly influenced by the dispersing agent, sodium dodecyl sulphate and Aloe Vera. The EDS and XPS analyses show that both synthetic routes produce the nanoscale MgO phase. FTIR spectra for MgO NPs annealed at different temperatures show slight changes in

intensity and small shifts in the vibration modes with increasing calcination temperature. Peaks appearing between 400–700 cm^{-1} confirm the presence of MgO at the nanoscale. The diffractograms of MgO NPs synthesized with the AVE precipitating agent showed an increase in the intensity of the diffraction planes without shifting the diffraction angles as the calcination temperature increased. A slight increase in crystallite size was observed compared to MgO NPs synthesized with the SDS precipitating agent. The absorption peaks of both MgO NPs exhibit a blue shift. The average crystallite size of commercial MgO nanoparticles is approximately twice that of those synthesized with the two dispersing agents.

Acknowledgments

This paper was financially supported by the Ministry of Education and Research of the Republic of Moldova, MSU, under the subprogram "Designing Supramolecular Architectures Based on Metal Phthalocyanine Derivatives and Functionalized Nanoparticles for Medical Applications," #011209, a project PN-IV-P8-8.3-ROMD-2023-0048 (DSUPRAMED), within PNCDI IV.

References

1. Li, H.; Li, M.; Qiu, G.; Li, C.; Qu, C.; Yang, B. Synthesis and characterization of MgO nanocrystals for biosensing applications. Journal of Alloys and Compounds, 2015, 632, pp. 639-644. DOI: https://doi.org/10.1016/j.jallcom.2015.01.294
2. Zheng, L.; Zhao, S.; Li, Y.; Xu, J.; Yan, W.; Guo, B.; Xu, J.; Jiang, L.; Zhang, Y.; Wei, H.; Jiang, Q. Engineered MgO nanoparticles for cartilage-bone synergistic therapy. Science Advances, 2024, 10, pp. 1–17. DOI: https://doi.org/10.1126/sciadv.adk6084
3. Mirzaei, H.; Davoodnia, A. Microwave assisted sol-gel synthesis of MgO nanoparticles and their catalytic activity in the synthesis of hantzsch 1,4-dihydropyridines. Chinese Journal of Catalysis, 2012, 33(9-10), pp. 1502–1507. DOI: https://doi.org/10.1016/S1872-2067(11)60431-2
4. Mohamad, E.A.; Shehata, A.M.; Abobah, A.M.; Kholief, A.T.; Ahmed, M.A.; Abdelhakeem, M.E.; Dawood, N.K.; Mohammed, H.S. Chitosan-based films blended with moringa leaves and MgO nanoparticles for application in active food packaging. International Journal of Biological Macromolecules, 2023, 253(6), 127045, pp. 1–20. DOI: https://doi.org/10.1016/j.ijbiomac.2023.127045
5. Gatou, M.; Skylla, E.; Dourou, P.; Pippa, N.; Gazouli, M.; Lagopati, N.; Pavlatou, E. Biomedical Applications of Magnesium Oxide Nanoparticles. Encyclopedia, 2024, pp. 1–18. https://encyclopedia.pub/entry/55554
6. Ramakrishna, L.; Thippeswamy, R.; Mallesh, G.K.; Kempahanumakkagari, S.K. Eco-friendly synthesis of novel magnesium oxide nanomaterials for dye degradation, battery, and sensor applications. Next Materials, 2024, 4, 100193, pp. 1–10. DOI: https://doi.org/10.1016/j.nxmate.2024.100193
7. Gatou, M.; Skylla, E.; Dourou, P.; Pippa, N.; Gazouli, M.; Lagopati, N.; Pavlatou, E. Magnesium oxide (MgO) nanoparticles: synthetic strategies and biomedical applications. Crystals, 2024, 14(3), 215, pp. 1–47. DOI: https://doi.org/10.3390/cryst14030215
8. Anand, K.V.; Anugraga, A.R.; Kannan, M.; Singaravelu, G.; Govindaraju, K. Bio-engineered magnesium oxide nanoparticles as nano-priming agent for enhancing seed germination and seedling vigour of green gram (*Vigna radiata* L.). Materials Letters, 2020, 271, 127792, pp. 1–4. DOI: https://doi.org/10.1016/j.matlet.2020.127792
9. Verma, S.K.; Nisha, K.; Panda, P.K.; Patel, P; Kumari, P.; Mallick, M.; Sarkar, B.; Das, B. Green synthesized MgO nanoparticles infer biocompatibility by reducing *in vivo* molecular nanotoxicity in embryonic zebrafish through arginine interaction elicited apoptosis. Science of the Total Environment, 2020, 713, 136521, pp. 1–12. DOI: https://doi.org/10.1016/j.scitotenv.2020.136521
10. Khan, A.; Shabir, D.; Ahmad, P.; Khandaker, M.; Faruque, M.; Din, I. Biosynthesis and antibacterial activity of MgO-NPs produced from Camellia-sinensis leaves extract. Materials Research Express, 2021, 8, 015402, pp. 1–11. DOI: https://doi.org/10.1088/2053-1591/abd421
11. Gliński, M.; Iwanek, E.; Ulkowska, U.; Czajka, A.; Kaszkur, Z. Catalytic activity of high-surface-area amorphous MgO obtained from upsalite. Catalysts, 2021, 11, 1338, pp. 1–14. DOI: https://doi.org/10.3390/catal11111338
12. Sun, L.; He, H.; Liu, C.; Ye, Z. Local super-saturation dependent synthesis of MgO nanosheets. Applied Surface Science, 2011, 257(8), 36073611, pp. 1–5. DOI: https://doi.org/10.1016/j.apsusc.2010.11.087
13. Kumar, A.; Thota, S.; Varma, S.; Kumar, J. Sol–gel synthesis of highly luminescent magnesium oxide nanocrystallites. Journal of Luminescence, 2011, 131(4), pp. 640–648. DOI: https://doi.org/10.1016/j.jlumin.2010.11.008
14. Li, M.; Wang, X.; Li, H.; Di, H.; Wu, X.; Fang, C.; Yang, B. Preparation of photoluminescent single crystalline MgO nanobelts by DC arc plasma jet CVD. Applied Surface Science, 2013, 274, pp. 188–194. DOI: https://doi.org/10.1016/j.apsusc.2013.03.013
15. Liu, J.L.; Li, C.M.; Chen, L.X.; Wei, J.J.; Hei, L.F.; Wang, J.J.; Feng, Z.H.; Guo, H.; Lv, F.X. Nucleation and growth surface conductivity of H-terminated diamond films prepared by DC arc jet CVD. Diamond and Related Materials, 2013, 32, pp. 48–53. DOI: https://doi.org/10.1016/j.diamond.2012.11.013
16. Yin, Y.; Zhang, G.; Xia, Y. Synthesis and characterization of MgO nanowires through a vapor-phase precursor method. Advanced Functional Materials, 2002, 12(4), pp. 293–298. DOI: https://doi.org/10.1002/1616-3028(20020418)12:4%3C293::AID-ADFM293%3E3.0.CO;2-U

17. Endla, P. Structure, morphology, and luminescence properties of sol–gel-synthesized pure and cobalt-doped MgO nanoparticles. Ionics, 2024, 30, pp. 7653–7663. DOI: https://doi.org/10.1007/s11581-024-05812-x
18. Rafique, M.; Sadaf, I.; Rafique, M.S.; Tahir, M.B. A review on green synthesis of silver nanoparticles and their applications. Artificial Cells, Nanomedicine, and Biotechnology, 2017, 45(7), pp. 1272–1291. DOI: https://doi.org/10.1080/21691401.2016.1241792
19. Bandeira, M.; Giovanela, M.; Roesch-Ely, M.; Devine, D.M.; Crespo, J.S. Green synthesis of zinc oxide nanoparticles: A review of the synthesis methodology and mechanism of formation. Sustainable Chemistry and Pharmacy, 2020, 15, 100223, pp. 1–10. DOI: https://doi.org/10.1016/j.scp.2020.100223
20. Yildiz, Y.; Okyay, T.; Sen, B.; Gezer, B.; Kuzu, S.; Savk, A.; Demir, E.; Dasdelen, Z.; H. Sert, H.; Sen, F. Highly monodisperse Pt/Rh nanoparticles confined in the graphene oxide for highly efficient and reusable sorbents for methylene blue removal from aqueous solutions. ChemistrySelect, 2017, 2(2), pp. 697–701. DOI: https://doi.org/10.1002/slct.201601608
21. Göksu, H.; Çelik, B.; Yıldız, Y.; Şen, F.; Kılbaş, B. Superior monodisperse CNT-supported CoPd (CoPd@CNT) nanoparticles for selective reduction of nitro compounds to primary amines with $NaBH_4$ in aqueous medium. ChemistrySelect, 2016, 1(10), pp. 2366–2372. DOI: https://doi.org/10.1002/slct.201600509
22. Sen, B.; Şavk, A.; Sen, F. Highly efficient monodisperse Pt nanoparticles confined in the carbon black hybrid material for hydrogen liberation. Journal of Colloid and Interface Science, 2018, 520, pp. 112–118. DOI: https://doi.org/10.1016/j.jcis.2018.03.004
23. Şen, B.; Aygün, A.; Şavk, A.; Akocak, S.; Şen, F. Bimetallic palladium-iridium alloy nanoparticles as highly efficient and stable catalyst for the hydrogen evolution reaction. International Journal of Hydrogen Energy, 2018, 43(44), pp. 20183–20191. DOI: https://doi.org/10.1016/j.ijhydene.2018.07.081
24. Seyama, H.; Soma, M. X-ray photoelectron spectroscopic study of montmorillonite containing exchangeable divalent cations. Journal of the Chemical Society, Faraday Transactions 1: Physical Chemistry in Condensed Phases, 1984, 80(1), pp. 237–248. DOI: https://doi.org/10.1039/F19848000237
25. Srivastava, V.; Sharma, Y.C.; Sillanpää, M. Green synthesis of magnesium oxide nanoflower and its application for the removal of divalent metallic species from synthetic wastewater. Ceramics International, 2015, 41(5B), pp. 6702–6709. DOI: https://doi.org/10.1016/j.ceramint.2015.01.112
26. Moulder, J.F.; Stickle, W.F.; Sobol, P.E. Handbook of X-ray Photoelectron Spectroscopy. Perkin-Elmer Corporation: Eden Prairie, 1993, 260 p.
27. Grindlay, D.; Reynolds, T. The *Aloe vera* phenomenon: A review of the properties and modern uses of the leaf parenchyma gel. Journal of Ethnopharmacology, 1986, 16(2-3), pp. 117–151. DOI: https://doi.org/10.1016/0378-8741(86)90085-1
28. Jeevanandam, J.; Chan, Y.S.; Danquah, M.K. Calcination-dependent morphology transformation of sol-gel- synthesized MgO nanoparticles. ChemistrySelect, 2017, 2(32), pp. 10393–10404. DOI: https://doi.org/10.1002/slct.201701911
29. Muhaymin, A.; Mohamed, H.E.A.; Hkiri, K.; Safdar, A.; Azizi, S.; Maaza, M. Green synthesis of magnesium oxide nanoparticles using *Hyphaene thebaica* extract and their photocatalytic activities. Scientific Reports, 2024, 14, 20135, pp. 1–12. DOI: https://doi.org/10.1038/s41598-024-71149-0
30. Ardizzone, S.; Bianchi, C.L.; Fadoni, M.; Vercelli, B. Magnesium salts and oxide: an XPS overview. Applied Surface Science, 1997, 119(3-4), pp. 253–259. DOI: https://doi.org/10.1016/S0169-4332(97)00180-3
31. Lee, S.M.; Ito, T.; Murakami, H. X-ray photoelectron spectroscopy characterization and morphology of MgO thin films grown on single-crystalline diamond (100). Journal of Materials Research, 2002, 17, pp. 1914–1922. DOI: https://doi.org/10.1557/JMR.2002.0284
32. Aswal, D.K.; Muthe, K.P.; Tawde, S.; Chodhury, S.; Bagkar, N.; Singh, A.; Gupta, S.K.; Yakhmi, J.V. XPS and AFM investigations of annealing induced surface modifications of MgO single crystals. Journal of Crystal Growth, 2002, 236(4), pp. 661–666. DOI: https://doi.org/10.1016/S0022-0248(02)00852-7
33. Balamurugan, S.; Ashna, L.; Parthiban, P. Synthesis of nanocrystalline MgO particles by combustion followed by annealing method using hexamine as a fuel. Journal of Nanotechnology, 2014, 841803, pp. 1–6. DOI: https://doi.org/10.1155/2014/841803
34. Sagaya Selvam, N.C.; Kumar, R.T.; Kennedy, L.J.; Vijaya, J.J. Comparative study of microwave and conventional methods for the preparation and optical properties of novel MgO-micro and nano-structures. Journal of Alloys and Compounds, 2011, 509(41), pp. 9809–9815. DOI: https://doi.org/10.1016/j.jallcom.2011.08.032
35. Praffulla, S.R.; Bubbly, S.G. Synthesis and characterization of Chitosan-CuO-MgO polymer nanocomposites. AIP Conference Proceedings, 2018, 1953(1), 030168, pp. 1–6. DOI: https://doi.org/10.1063/1.5032503
36. Ercan, I.; Kaygili, O.; Ates, T.; Gunduz, B.; Bulut, N.; Koytepe, S.; Ozcan, I. The effects of urea content on the structural, thermal and morphological properties of MgO nanopowders. Ceramics International, 2018, 44(12), pp. 14523–14527. DOI: https://doi.org/10.1016/j.ceramint.2018.05.068
37. Saidi, N.S.M.; Ying, K.J.; Yusoff, H.M.; Badar, N. Synthesis and characterization of magnesium oxide nanoparticles by using banana peel (*Musa acuminata* cavendish) extract. Malaysian Journal of Analytical Sciences, 2023, 27(5), pp. 1017–1034. https://mjas.analis.com.my/mjas/v27_n5/pdf/Mohd%20Saidi_27_5_9.pdf
38. Kumari, S.V.G.; Pakshirajan, K.; Pugazhenthi, G. Synthesis and characterization of MgO nanostructures: A comparative study on the effect of preparation route. Materials Chemistry and Physics, 2023, 294, 127036, pp. 1–14. DOI: https://doi.org/10.1016/j.matchemphys.2022.127036